

## Photoelectrochemistry by Design: Tailoring the Nanoscale Structure of Pt/NiO Composites Leads to Enhanced Photoelectrochemical Hydrogen Evolution Performance

András Sápi, Andras Varga, Gergely Ferenc Samu, Dorina G. Dobó, Koppány L. Juhász, Bettina Takacs, Erika Varga, Akos Kukovecz, Zoltán Kónya, and Csaba Janáky

*J. Phys. Chem. C*, **Just Accepted Manuscript** • DOI: 10.1021/acs.jpcc.7b00429 • Publication Date (Web): 05 Apr 2017

Downloaded from <http://pubs.acs.org> on April 7, 2017

### Just Accepted

“Just Accepted” manuscripts have been peer-reviewed and accepted for publication. They are posted online prior to technical editing, formatting for publication and author proofing. The American Chemical Society provides “Just Accepted” as a free service to the research community to expedite the dissemination of scientific material as soon as possible after acceptance. “Just Accepted” manuscripts appear in full in PDF format accompanied by an HTML abstract. “Just Accepted” manuscripts have been fully peer reviewed, but should not be considered the official version of record. They are accessible to all readers and citable by the Digital Object Identifier (DOI®). “Just Accepted” is an optional service offered to authors. Therefore, the “Just Accepted” Web site may not include all articles that will be published in the journal. After a manuscript is technically edited and formatted, it will be removed from the “Just Accepted” Web site and published as an ASAP article. Note that technical editing may introduce minor changes to the manuscript text and/or graphics which could affect content, and all legal disclaimers and ethical guidelines that apply to the journal pertain. ACS cannot be held responsible for errors or consequences arising from the use of information contained in these “Just Accepted” manuscripts.

1  
2  
3 **Photoelectrochemistry by Design: Tailoring the Nanoscale Structure of**  
4  
5 **Pt/NiO Composites Leads to Enhanced Photoelectrochemical Hydrogen**  
6  
7 **Evolution Performance**  
8  
9

10  
11  
12  
13 András Sápi<sup>a</sup>, András Varga<sup>b,c</sup>, Gergely F. Samu<sup>b,c</sup>, Dorina Dobó<sup>a</sup>, Koppány L. Juhász<sup>a</sup>,  
14 Bettina Takács<sup>b,c</sup>, Erika Varga<sup>c</sup>, Ákos Kukovecz<sup>a,d</sup>, Zoltán Kónya<sup>a,c</sup>, and Csaba Janáky<sup>b,c,\*</sup>  
15  
16

17  
18  
19  
20 <sup>a</sup>Department of Applied and Environmental Chemistry, University of Szeged, Rerrich Square  
21 1, Szeged, H-6720, Hungary  
22

23 <sup>b</sup>MTA-SZTE „Lendület” Photoelectrochemistry Research Group, Rerrich Square 1, Szeged,  
24 H-6720, Hungary  
25

26 <sup>c</sup>Department of Physical Chemistry and Materials Science, University of Szeged, Rerrich  
27 Square 1, Szeged, H-6720, Hungary  
28

29 <sup>d</sup>MTA-SZTE „Lendület” Porous Nanocomposites Research Group, Rerrich Square 1, Szeged,  
30 H-6720, Hungary  
31

32 <sup>e</sup>MTA-SZTE Reaction Kinetics and Surface Chemistry Research Group, Rerrich Square 1.,  
33 Szeged H-6720, Hungary  
34  
35  
36  
37  
38

39 \*Corresponding author, e-mail: [janaky@chem.u-szeged.hu](mailto:janaky@chem.u-szeged.hu)  
40  
41  
42  
43  
44  
45  
46  
47  
48  
49  
50  
51  
52  
53  
54  
55  
56  
57  
58  
59  
60

**Abstract**

Photoelectrochemical hydrogen evolution is a promising avenue to store the energy of sunlight in the form of chemical bonds. The recent rapid development of new synthetic approaches enables the nanoscale engineering of semiconductor photoelectrodes, thus tailoring their physico-chemical properties towards efficient H<sub>2</sub> formation. In this work we carried out the parallel optimization of the morphological features of the semiconductor light absorber (NiO) and the co-catalyst (Pt). While nanoporous NiO films were obtained by electrochemical anodization, the monodisperse Pt nanoparticles were synthesized using wet chemical methods. The Pt/NiO nanocomposites were characterized by XRD, XPS, SEM, ED, TEM, cyclic voltammetry, photovoltammetry, EIS, etc. The relative enhancement of the photocurrent was demonstrated as a function of the nanoparticle size and loading. For mass-specific surface activity the smallest nanoparticles (2.0 and 4.8 nm) showed the best performance. After de-convoluting the trivial geometrical effects (stemming from the variation of Pt particle size and thus the electroactive surface area), however, the intermediate particle sizes (4.8 and 7.2 nm) were found to be optimal. Under optimized conditions, a twenty-fold increase in the photocurrent (and thus the H<sub>2</sub> evolution rates) was observed for the nanostructured Pt/NiO composite, compared to the benchmark nanoparticulate NiO film.

## Introduction

With the rapidly increasing global renewable energy harvesting capacities there is a rising interest for energy storage solutions, to overcome the intermittent nature of the various renewable energy sources. Photoelectrochemical (PEC) H<sub>2</sub> evolution reaction (HER) and CO<sub>2</sub> conversion are both promising avenues to generate solar fuels and thus store the energy of sunlight in the form of chemical bonds.<sup>1,2</sup> One of such PEC procedures is the direct reduction of H<sup>+</sup> ions at the interface of a p-type semiconductor (SC) photocathode and a liquid electrolyte. Alternatively, when irradiating an n-type SC, water oxidation occurs at the SC/electrolyte interface, while HER can proceed on the counterelectrode. A range of photocathodes has been screened during the past decades,<sup>3-6</sup> and reasonable solar to hydrogen conversion efficiencies have been achieved employing complex electrode assemblies.<sup>7,8</sup> At the same time, there are still several open questions to be answered before high activity, stability, and selectivity could be achieved at the same time.<sup>9</sup>

Recent studies indicated that the use of nanostructured photoelectrodes may help to enhance electron transfer rates to levels which make practical significance.<sup>10,11</sup> While the high specific area (i.e., roughness factor) is a key advantage in electrocatalysis, the picture is much murkier in the photo-electrocatalytic scenario, because nanostructuring of photoelectrodes has both benefits and drawbacks. For example, charge carrier recombination due to both surface traps and the necessity of hopping from one particle to another, certainly decreases the achievable solar to chemical conversion efficiencies. Interconnected nanostructures may help to circumvent this issue, by eliminating the need of interparticle charge transfer. Different examples can be cited, ranging from mesoporous TiO<sub>2</sub> vs. TiO<sub>2</sub> nanotubes,<sup>12,13</sup> nanoparticulate and nanoporous WO<sub>3</sub>,<sup>14,15</sup> and so forth.

NiO has been increasingly studied as a photocathode material, recently. NiO may also have practical significance in p-type DSSCs, in an inverted configuration compared to its

1  
2  
3 TiO<sub>2</sub>-based counterpart.<sup>16-18</sup> Interestingly, although the NiO is long known to be capable of  
4 both evolving H<sub>2</sub> and reducing CO<sub>2</sub> (based on its conduction band edge position)<sup>19</sup>, its solar  
5 fuel generation ability has not been extensively studied. There are a few examples, where NiO  
6 was studied in conjunction with either a solid state or molecular co-catalyst, in HER and CO<sub>2</sub>  
7 ER. For example, a NiO/Cu<sub>2</sub>O heterojunction was employed as both light absorber and H<sub>2</sub>-  
8 evolution catalyst.<sup>20</sup> In another study, NiO was decorated with a Ru-dye and Ni catalyst to  
9 achieve visible light driven PEC H<sub>2</sub>-evolution.<sup>21</sup> PEC CO<sub>2</sub> conversion to CO was  
10 demonstrated in combination with a Ru(II)-Re(I) containing supramolecular catalyst.<sup>22</sup> With  
11 respect to morphological questions, the PEC behavior of a nanoparticulate NiO film was  
12 compared with compact NiO recently, with special focus on their characterization with  
13 surface photovoltage spectroscopy.<sup>23</sup> On the other hand, there is only one single report on the  
14 PEC properties of interconnected NiO nanostructures.<sup>24</sup> The versatility of NiO is reflected in  
15 the fact that it has been also studied as protective coating for Si photoanodes, in solar fuel  
16 generation processes.<sup>25,26</sup>

17  
18  
19  
20  
21  
22  
23  
24  
25  
26  
27  
28  
29  
30  
31  
32  
33  
34  
35  
36  
37  
38  
39  
40  
41  
42  
43  
44  
45  
46  
47  
48  
49  
50  
51  
52  
53  
54  
55  
56  
57  
58  
59  
60

Combination of a SC light absorber with a metal electrocatalyst is a promising avenue to further enhance the solar to chemical conversion efficiency, because the light absorption and charge transfer is decoupled. Consequently, by intimately linking an electrocatalyst to the SC surface a Schottky-junction can be formed, which in turn facilitates the rapid charge carrier extraction from the SC to the metal co-catalyst.<sup>27,28</sup> PEC H<sub>2</sub>-evolution takes place in the next step, on the surface of the metal nanoparticle co-catalyst. While various co-catalysts have been examined,<sup>29</sup> Pt is still considered as the state-of-the-art electrocatalyst for the EC hydrogen evolution.

The effect of Pt size was studied in different electrocatalytic processes. For example, in oxygen reduction reaction (ORR) the mass specific activity was increased sharply in the range of 1.2 – 2.2 nm Pt particles and slightly decreased for even larger particle sizes (>2.5

1  
2  
3 nm).<sup>30</sup> In another study CO electrooxidation was studied on Pt nanoparticles ranging from 1-  
4  
5 30 nm, and the importance of particle shape and specific adsorption was also highlighted.<sup>31</sup>  
6  
7 Similarly, Pt has been heavily studied and utilized as (co-)catalyst in both thermally- and  
8  
9 photo-activated heterogeneous catalysis. The effect of Pt nanoparticle size (diameter of 1-10  
10  
11 nm) on their heterogeneous catalytic activity was studied for both gas and liquid phase  
12  
13 reactions. For example, in the case of alcohol oxidation, larger particles had higher activity  
14  
15 towards the formation of aldehydes, ketones, and carbon-dioxide.<sup>32-34</sup> For benzene and  
16  
17 toluene hydrogenation, ~2-3 nm sized Pt nanoparticles had outstanding activity compared to  
18  
19 both smaller and larger nanoparticles.<sup>35</sup> In photocatalytic hydrogen evolution (using oxalic  
20  
21 acid as sacrificial e<sup>-</sup> donor) over TiO<sub>2</sub> supported Pt nanoparticles, 3 nm sized particles showed  
22  
23 the best activity compared to both smaller and bigger particles.<sup>36</sup> Photodriven CO<sub>2</sub> reduction  
24  
25 was performed on TiO<sub>2</sub>/Pt composites, containing photodeposited ultrasmall Pt nanoparticles  
26  
27 (below 2 nm).<sup>37</sup> The particle size and density on the PEC performance was also studied for  
28  
29 Pt/Si samples, involving relatively large Pt particles (40-300 nm) on flat Si electrodes.<sup>38</sup>  
30  
31  
32  
33

34 Taking all the above listed precedencies as a whole, it is clear that there is  
35  
36 considerable scope for the nanoscale engineering of both the light absorber and the co-catalyst  
37  
38 in metal/SC composite electrodes. In this paper we report on high PEC H<sub>2</sub> generation rates on  
39  
40 optimized Pt/NiO nanostructures. We studied the effect of the NiO nanostructure as well as  
41  
42 the Pt co-catalyst size (and loading), where we found that there is an optimal particle size and  
43  
44 loading. Under properly adjusted conditions, a twenty-fold increase in the photocurrent (and  
45  
46 thus the H<sub>2</sub> evolution rates) was observed compared to the benchmark nanoparticulate NiO  
47  
48 film. Finally, we verified that particle size of the co-catalyst in a PEC configuration is equally  
49  
50 important as it was in the previously studied electrocatalytic and photocatalytic scenarios.<sup>30-35</sup>  
51  
52  
53

## 54 **Experimental Section**

### 55 **Materials**

1  
2  
3 For the anodization experiments Ni foils (99.9+%, 0.125 mm thick),  $\text{NH}_4\text{F}$  ( $\geq 99\%$ ),  
4 ethylene glycol ( $\geq 99\%$ ) were all purchased from Sigma-Aldrich, and KOH ( $\geq 86\%$  in water)  
5 from Fluka. For cleaning the metal foils ethanol (Chromanorm) 2-propanol (Chromanorm),  
6 and acetone (Rectapur) were purchased from VWR. For the electrochemical measurements  
7  $\text{Na}_2\text{SO}_4$  (99%, Alfa Aesar) was used, along with  $\text{N}_2$  gas (99.995%, Messer, Budapest,  
8 Hungary). All solutions were prepared with ultrapure water (Milli-Q,  $\rho=18.2 \text{ M}\Omega \text{ cm}$ ). All  
9 chemical reagents were used without further purification.  
10  
11  
12  
13  
14  
15  
16  
17

### 18 **Anodization of the Ni foil**

19  
20 Prior to anodization, the Ni foils were mechanically polished to mirror finish using  
21 silicon carbide sandpaper with successively finer roughness. To ensure the removal of any  
22 attached organic contaminants three subsequent steps (5 min) of ultrasonication in acetone, 2-  
23 propanol, and finally ultrapure water were performed. The anodization was carried out in a  
24 standard two-electrode setup, where the Ni foil acted as the anode and a Pt foil as the cathode.  
25 The Ni foil was pressed between two O-rings, leaving  $2.27 \text{ cm}^2$  exposed to the electrolyte,  
26 while the electric contact was located on the back of the sample. The anodization was carried  
27 out at different voltages using a programmable DC power supply (Voltcraft PSP 1803), while  
28 the procedure was monitored by a digital multimeter (Keithley 2000). Both instruments were  
29 controlled by custom-written LabVIEW software. Immediately after the anodization, the  
30 samples were carefully washed with ultrapure water and dried in  $\text{N}_2$  stream. To obtain the  
31 desired crystalline phase of NiO, the anodized samples were annealed for 4 h at  $500 \text{ }^\circ\text{C}$ , with  
32 a heating ramp of  $10 \text{ }^\circ\text{C min}^{-1}$  (Thermo Scientific Heraeus K114 Furnace).  
33  
34  
35  
36  
37  
38  
39  
40  
41  
42  
43  
44  
45  
46  
47  
48

49 Three different electrolyte compositions were used (the first two were adopted from the  
50 literature)<sup>24,39</sup> to perform the anodization:  
51  
52

- 53 (i) aqueous solution consisting of 0.5 M  $\text{NH}_4\text{F}$  dissolved in 85 wt%  $\text{H}_3\text{PO}_4$ , with an  
54 anodization voltage of 6 V - 10 V, for 10 min.<sup>39</sup>  
55  
56  
57  
58  
59  
60

- 1  
2  
3 (ii) organic media consisting of 0.5 wt% KOH, 5 wt% H<sub>2</sub>O, and 94,5 wt% ethylene  
4 glycol with an anodization voltage of 40 V-60 V and duration of 1 hour.<sup>24</sup>  
5  
6  
7 (iii) a combined electrolyte consisting of an ethylene glycol solution containing 0.15 M  
8 KOH, 0.1 M NH<sub>4</sub>F, and 3 V/V% H<sub>2</sub>O. During these syntheses the voltage was  
9 held at 30 V for 1 hour.  
10  
11  
12

### 13 14 **Preparation of Pt nanoparticles**

15  
16 Pt nanoparticles with various sizes were synthesized as described in the Supporting  
17 Information.<sup>34</sup> Briefly, NaOH and polyvinylpyrrolidone ( $M_w = 29,000$ ) were dissolved in  
18 ethylene glycol together with the platinum precursor ( $H_2PtCl_6 \cdot xH_2O$  or platinum(II)  
19 acetylacetonate). Subsequently, the mixture was heated to 160-200 °C in an oil bath and held  
20 at that temperature between 10 min and 2 h under Argon atmosphere. Pt nanoparticles in five  
21 different sizes were synthesized, with a diameter of  $2.0 \pm 0.4$ ,  $4.8 \pm 0.7$ ,  $7.2 \pm 0.8$ ,  $8.6 \pm 1.3$ , and  
22  $12.3 \pm 1.4$  nm. The resulting Pt nanoparticles were precipitated with acetone, centrifuged and  
23 dispersed in ethanol. Finally, the nanoparticles were repeatedly washed with hexane,  
24 centrifuged, and re-dispersed in ethanol before use. The exact concentration of the Pt  
25 suspensions was determined by ICP-MS measurements (Agilent 7700x type ICP-MS  
26 spectrometer).  
27  
28  
29  
30  
31  
32  
33  
34  
35  
36  
37  
38  
39

### 40 **Drop-casting of Pt on the NiO films**

41  
42 First the NiO samples were cut into four pieces with equivalent geometric areas of  
43  $0.57 \text{ cm}^2$  to minimize the possible error arising from the use of different samples. One piece  
44 was always kept as an internal reference and every normalization was carried out with respect  
45 to this. The suspension of different sized Pt nanoparticles was prepared in ethanol (sonicated  
46 for 60 min) and was then drop-casted on the surface of the NiO samples (preheated on a  
47 hotplate at 65 °C). Investigations were carried out with different Pt loadings ( $0.5 - 4.0 \mu\text{g cm}^{-2}$ ).  
48 To improve the adherence between the Pt nanoparticles and the NiO scaffold, and to  
49  
50  
51  
52  
53  
54  
55  
56  
57  
58  
59  
60

1  
2  
3 remove the capping polyvinylpyrrolidone from the Pt surface, the as prepared NiO/Pt  
4  
5 composites were annealed in air at 300 °C for 2 hours with a heating ramp of 5 °C min<sup>-1</sup>.  
6

### 7 **Physical characterization**

8  
9 The X-ray diffraction (XRD) patterns were recorded with a Rigaku MiniFlex II  
10 benchtop instrument with Cu K $\alpha$  X-ray source ( $\lambda = 1.5406 \text{ \AA}$ ), in the 20 - 80° range, with a 2°  
11 min<sup>-1</sup> scan rate. Raman spectra were recorded with a Thermo Scientific<sup>TM</sup> DXR<sup>TM</sup> Raman  
12 microscope at an excitation wavelength of 532 nm, applying 10 mW laser power, and  
13 averaging 20 spectra with an exposition time of 6 seconds. Scanning electron microscopic  
14 (SEM) images were captured using a Hitachi S4700 FE-SEM instrument. Transmission  
15 electron microscopic (TEM) investigation and electron diffraction analysis were performed  
16 using a FEI Tecnai<sup>TM</sup> G<sup>2</sup> 20 X-Twin type instrument, operating at an acceleration voltage of  
17 200 kV. The Pt containing ethanol based suspensions were drop-casted on carbon film coated  
18 copper grids. In the case of the NiO samples, a small part of the surface of the electrode  
19 materials was scratched into a tiny jar filled with ethanol before ultrasonication. X-ray  
20 photoelectron spectra were recorded with a SPECS instrument equipped with a PHOIBOS  
21 150 MCD 9 hemispherical analyzer. The analyzer was operated in the fixed analyzer  
22 transmission (FAT) mode with 20 eV pass energy. The Al K $\alpha$  radiation ( $h\nu = 1486.6 \text{ eV}$ ) of a  
23 dual anode X-ray gun was used as an excitation source. The gun was operated at 210 W  
24 power (14 kV, 15 mA). The binding energy scale was corrected by fixing the main C 1s  
25 component to 285.0 eV, corresponding to the adventitious carbon. For spectrum acquisition  
26 and evaluation both manufacturers (SpecsLab2) and commercial (CasaXPS, Origin) software  
27 packages were used.  
28  
29  
30  
31  
32  
33  
34  
35  
36  
37  
38  
39  
40  
41  
42  
43  
44  
45  
46  
47  
48  
49  
50

### 51 **Electrochemical measurements**

52 All electrochemical measurements were performed using an Autolab PGSTAT302N  
53 instrument equipped with an FRA32M module. The measurements were carried out in a  
54  
55  
56  
57  
58  
59  
60

1  
2  
3 standard three electrode setup, where the studied Pt/NiO acted as working electrode, a  
4 platinum foil and Ag/AgCl (satd. NaCl) electrode were used as the counter and the reference  
5 electrodes, respectively. The electrolyte was purged with N<sub>2</sub> gas for 20 min before each  
6 measurement.  
7  
8  
9

10  
11 Photoelectrochemical measurements were carried out in a sealed two compartment,  
12 quartz cell where 0.1 M Na<sub>2</sub>SO<sub>4</sub> solution was used as the electrolyte. Linear sweep  
13 voltammograms were recorded from 0.0 V to -1.0 V with a sweep rate of 2 mV s<sup>-1</sup> under  
14 periodically chopped illumination (0.1 Hz). The light source was a 300 W Hg-Xe arc lamp  
15 (Hamamatsu L8251). The radiation source was placed 3 cm away from the working electrode  
16 surface. When performing the long-term PEC measurements, the potential was held at E= -0.8  
17 V, the solution was stirred continuously, and the solution temperature was kept constant at  
18 25 °C. In these experiments the gas phase products were detected with a gas chromatograph  
19 (Shimadzu GC-2010 Plus equipped with a barrier ionization discharge (BID) detector).  
20  
21  
22  
23  
24  
25  
26  
27  
28  
29  
30  
31

32 For the electrochemical impedance spectroscopy (EIS) measurements a closed  
33 electrochemical cell was employed, where 1.0 M Na<sub>2</sub>SO<sub>4</sub> solution was used as the electrolyte.  
34 Prior to each EIS measurement, five cyclic voltammetry (CV) scans were recorded in the  
35 range of -0.8 V to 1.0 V with a 50 mV s<sup>-1</sup> sweep rate to ensure proper wetting of the porous  
36 electrodes and to estimate the electroactive surface area of the Pt nanoparticles. All  
37 impedance spectra were recorded at two different potential values (E= 0.0 V and E= -0.6 V),  
38 in the 10 Hz to 0.1 MHz frequency range, using a sinusoidal excitation signal (10 mV RMS  
39 amplitude).  
40  
41  
42  
43  
44  
45  
46  
47  
48

49 Incident photon-to-electron conversion efficiency (IPCE) measurements were  
50 performed on a Newport Quantum Efficiency Measurement System (QEPVSI-B) in a single-  
51 compartment, three electrode quartz electrochemical cell. The wavelength range was 250-400  
52  
53  
54  
55  
56  
57  
58  
59  
60

1  
2  
3 nm ( $\Delta\lambda = 10$  nm step size). The IPCE profiles were recorded in a 0.2 M Na<sub>2</sub>SO<sub>4</sub> solution at E  
4  
5 = -0.8 V bias potential.  
6

## 7 8 **Results and Discussion**

### 9 **Anodization of Ni foils**

10  
11 As described in the Experimental Section, anodization of Ni foils was carried out in  
12  
13 three different complexing agent containing media. The first method employed F<sup>-</sup> ions,  
14  
15 dissolved in concentrated H<sub>3</sub>PO<sub>4</sub> media.<sup>39</sup> Different anodization voltages were used, and by  
16  
17 increasing the applied voltage, the gradual increase of the steady-state current was observed  
18  
19 (Figure S1). This trend is related to the rate of the dissolution of the metal-oxide layer<sup>24</sup>, and  
20  
21 also affects the pore size of the obtained porous electrodes.<sup>40</sup> The samples prepared at 6 V  
22  
23 showed a compact morphology, whereas the presence of nanopores was observed at higher  
24  
25 anodization voltages (see SEM images in Figure S2). Unfortunately, this method led to F and  
26  
27 P-impurities in the structure (see further discussion and EDX data in Figure S3A), which  
28  
29 deleteriously affected the PEC response of the prepared electrodes (Figure S3B). To prevent  
30  
31 the incorporation of the phosphate impurity, our attention shifted to a method employing a  
32  
33 glycerol based media with KOH as the complexing agent.<sup>24</sup> In this case however, the high  
34  
35 etching rate of the formed NiO layer was observed (hindering morphology control), which  
36  
37 eventually lead to the complete dissolution of the Ni foils. To combat both the phosphate  
38  
39 inclusion and the fast dissolution of the formed NiO, a complex media was employed. The  
40  
41 optimized synthesis media consisted of ethylene glycol as the solvent, which contained 0.15  
42  
43 M KOH, 0.1 M NH<sub>4</sub>F, and 3 V/V% H<sub>2</sub>O.  
44  
45  
46  
47

48  
49 The use of organic solvent necessitated higher anodization voltages compared to the  
50  
51 aqueous synthesis (because of higher solution resistance). As the anodization voltage was  
52  
53 increased, faster NiO etching was observed (Figure 1A). Another typical feature of the  
54  
55 anodization curves was the appearance of a distinct current density maximum.<sup>41,42</sup> This can be  
56  
57 attributed to the increasing electrode surface area caused by the extensive pore formation.  
58  
59  
60

When the two competing reactions (oxide formation and dissolution) reach a steady state level however, near-constant current densities stabilized at the later stages of anodization.

SEM images were recorded to probe the morphology of the NiO films obtained at different anodization voltages. The nanoporous morphology was witnessed for all samples, but the pore size was found to be dependent from the anodization voltage (Figure 1B and Figure S5). On the high magnification SEM image, the interconnected nanoporous structure can be observed (Figure 1B). The size of the obtained pores fall into the range of  $15\pm 5$  nanometers (see pore size distribution in Figure 1C), while the grain size was slightly larger ( $\sim 20$  nm, see also TEM images later in Figure 7). These morphological features show close resemblance to the porous NiO electrodes prepared in fluoride containing electrolytes (1. method). We note here that in the case of the glycerol-based alkaline method the formation of macroporous structures were reported.<sup>24</sup> In all further experiments the samples prepared at  $U=30$  V for 1 h anodization time were used.

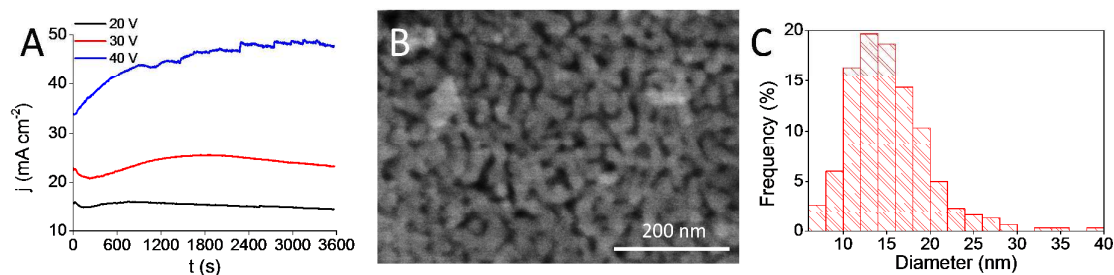
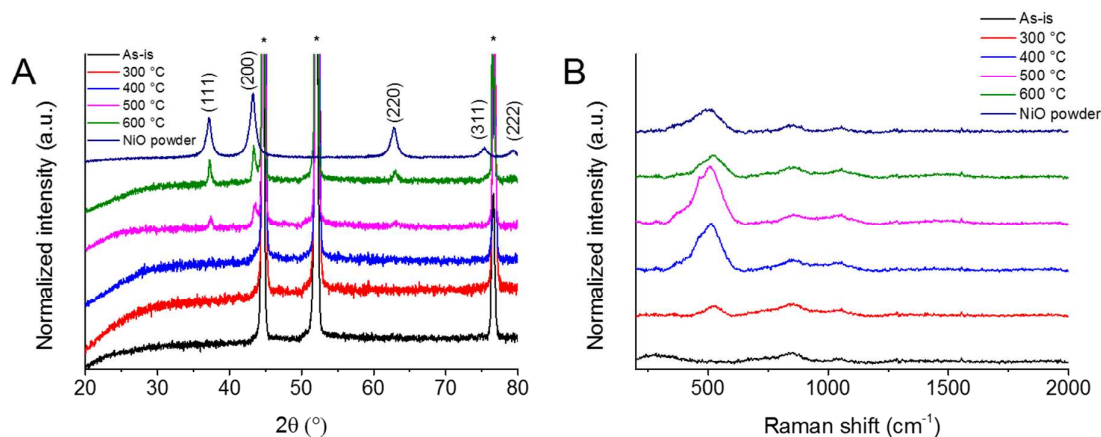


**Figure 1.** **A:** The effect of applied voltage on the anodization traces recorded in 0.15 M KOH, 0.1 M NH<sub>4</sub>F, and 3 V/V% H<sub>2</sub>O containing ethylene glycol. **B:** SEM image of the heat treated ( $T=500$  °C, 1h) NiO sample obtained at  $U=30$  V, 1 h. **C:** Pore size distribution of a typical NiO sample ( $U=30$  V, 1 h) annealed at  $T=500$ °C for 1 h.

Electrochemical anodization usually results in the formation of amorphous oxides materials, thus a subsequent heat treatment step is often necessary. To investigate the effect of heat treatment (300-600 °C) on the crystallinity of the samples, XRD measurements were carried out (Figure 2A). XRD profiles of the pristine NiO and a commercial NiO powder were also included as reference. The pristine anodized sample exhibited no reflections attributable

1  
2  
3 to NiO, only sharp reflections of the Ni foil underneath the amorphous layer were observed  
4 (marked with an asterisk). By employing a heat treatment above 500 °C, the development of  
5 the most intense reflections of NiO (JCPDS #47-1049) was observed. The average size of the  
6 crystalline domains was estimated using the Scherrer equation for the most intensive (111),  
7 diffraction. A  $d = 22$  nm value was obtained, very similar to the grain size obtained from the  
8 SEM images, which in turn confirms that the samples are fairly crystalline.

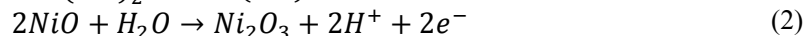
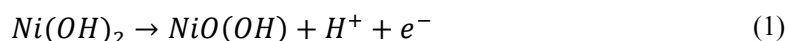
9  
10  
11  
12  
13  
14  
15  
16 To further investigate the structural features of the formed NiO layers Raman  
17 measurements were carried out (Figure 2B). The reference NiO powder exhibits three  
18 distinguishable Raman active vibration modes, which correspond to one-phonon LO modes  
19 (at  $\sim 513$   $\text{cm}^{-1}$ ), two-phonon TO + LO (at  $\sim 851$   $\text{cm}^{-1}$ ) and 2LO (at  $\sim 1048$   $\text{cm}^{-1}$ ) modes,  
20 respectively. These values are in close agreement with the reported values in the literature.<sup>43</sup>  
21  
22  
23  
24  
25  
26  
27 Furthermore, increasing heat treatment temperature, the gradual evolution of the LO mode  
28 was observed. While this vibrational mode is missing in the case of the unannealed (as is)  
29 sample, it is immediately observable even after a heat treatment at 300 °C. Based on the  
30 results from XRD and Raman spectroscopic measurements a heat treatment temperature of  
31 500 °C was chosen for future studies. EDX measurements (Figure S4), however detected  
32 some residual carbon in the samples annealed for 1 h, thus the heat treatment step was  
33 extended to 4h.  
34  
35  
36  
37  
38  
39  
40  
41  
42  
43



1  
2  
3 **Figure 2. A:** XRD patterns recorded for the anodized NiO samples (U= 30 V, 1 h) heat  
4 treated at different temperatures for 1 h and the reference NiO powder. **B:** Raman spectra  
5 recorded for the nanoporous NiO samples (U= 30 V, 1 h) heat treated at different  
6 temperatures and the reference NiO powder.  
7

### 8 **Electrochemical measurements**

9  
10 To evaluate the electrochemical behavior of the prepared nanoporous NiO electrodes  
11 cyclic voltammograms were recorded (Figure 3A). As reference measurements, NiO powder  
12 spray-coated on a glassy carbon electrode (Figure 3B) and a compact NiO layer (Figure 3C)  
13 (obtained by replacing the complexing agents in the anodization media with Na<sub>2</sub>SO<sub>4</sub>) were  
14 also studied. NiO usually exhibits two distinct redox peak pairs.<sup>44</sup> The first oxidation peak at  
15 E= 0.3 V is attributed to the oxidation of Ni(OH)<sub>2</sub> to various NiO(OH) phases (Equation 1).<sup>44</sup>  
16 The exact reaction however, involves different phases of NiO(OH) as described by the Bode-  
17 model.<sup>45</sup> The second oxidation peak starting at E> 0.75 V is related to the oxidation of Ni(II)  
18 to Ni(III) (Equation 2).<sup>23</sup>  
19  
20  
21  
22  
23  
24  
25  
26  
27  
28  
29



32  
33 In our case, only one broad anodic redox wave was seen centered at E~ 0.4 V,  
34 attributed to the redox transformation of Ni(OH)<sub>2</sub> to various NiO(OH) phases. By determining  
35 the charge capacitance values, it was found that the nanoporous NiO sample surpasses both  
36 the spray-coated NiO nanopowder (3-fold increase) and the NiO compact layer (27-fold  
37 increase) in term of electroactivity. This enhanced behavior can be mainly attributed to the  
38 superior surface area (vs. the compact layer) and the interconnected structure (vs.  
39 nanoparticulate films) of the anodized NiO samples. These observations already projected that  
40 the nanoporous NiO films will be a viable platform for future PEC studies.  
41  
42  
43  
44  
45  
46  
47  
48  
49  
50  
51  
52  
53  
54  
55  
56  
57  
58  
59  
60

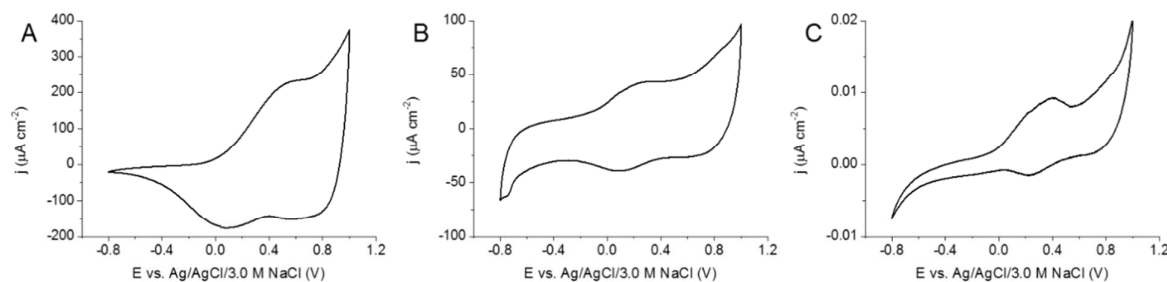


**Figure 3.** Cyclic voltammograms recorded in 0.2 M Na<sub>2</sub>SO<sub>4</sub> with 50 mV s<sup>-1</sup> sweep rate for: **A:** nanoporous NiO sample (prepared at U= 30 V, 1 h; heat treated at T= 500 °C, 4 h). **B:** NiO powder on glassy carbon electrode. **C:** compact NiO layer (prepared at U= 30 V, no complexing agent, 1 h; heat treated at T= 500 °C, 4 h).

### Photoelectrochemical measurements

To evaluate the photoresponse of the anodized NiO electrodes linear sweep photovoltammetry measurements were carried out (Figure 4). During illumination, the measured cathodic currents indicated a p-type semiconductor behavior of all studied samples. In these cases, no electron scavenger species was added, thus the photoresponse can be mainly ascribed to the photoreduction of water. Compared to the anodized and heat treated NiO layer (Figure 4A), both the spray-coated NiO nanopowder (Figure 4B) and the compact NiO layer (Figure 4C) showed inferior photoactivity (note the difference in the scale bar of the current density). In the latter two cases this may be the result of inadequate charge carrier extraction. As for the powdered sample, extensive charge carrier recombination may occur on the surfaces of the nanoparticles, which ultimately limits the photoresponse of this material. The case for the compact sample is somewhat different. Although the interfaces between particles are absent, the photogenerated carriers on the surface of the layer cannot be extracted through the bulk of the oxide (note the low conductivity of NiO). Thus, it can be concluded that the anodized sample exhibits superior PEC performance because of its interconnected nanoporous structure.

A further decisive parameter dictating the photoresponse of a material is its crystallinity. In Figure 4A the photoresponse of the anodized NiO samples heat treated at two

different temperatures are compared. The sample annealed at 300 °C, which exhibited no crystalline features, showed negligible photocurrents, while the sample heat treated at 500 °C showed  $j_{ph} = -80 \mu\text{A cm}^{-2}$  at  $E = -0.7 \text{ V}$ .

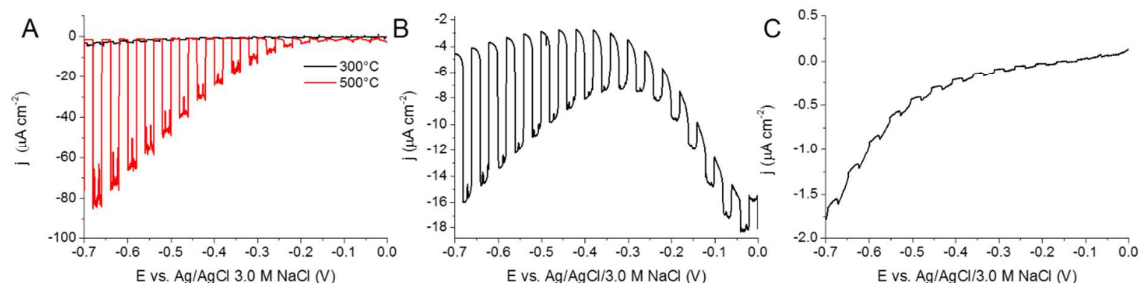


**Figure 4.** Linear sweep photovoltammograms recorded in 0.2 M  $\text{Na}_2\text{SO}_4$  with  $2 \text{ mV s}^{-1}$  sweep rate for: **A:** nanoporous NiO sample (prepared at  $U = 30 \text{ V}$ , 1 h; heat treated at  $T = 500 \text{ °C}$  and  $300 \text{ °C}$ , 4 h). **B:** NiO powder on glassy carbon electrode. **C:** compact NiO layer (prepared at  $U = 30 \text{ V}$ , 1 h; heat treated at  $T = 500 \text{ °C}$ , 4 h).

#### Pt decoration of the NiO electrodes

Pt nanoparticles with controlled size were synthesized in ethylene glycol by the polyol method using different Pt-based precursors and polyvinylpyrrolidone (PVP) as a capping agent (for more details see Supporting Information). The as-prepared Pt nanoparticles have narrow size distribution with an average diameter of  $2.0 \pm 0.4 \text{ nm}$ ,  $4.8 \pm 0.7 \text{ nm}$ ,  $7.2 \pm 0.8 \text{ nm}$ ,  $8.6 \pm 1.3 \text{ nm}$ ,  $12.3 \pm 1.4 \text{ nm}$  (Figure 5). This allowed to cover the 1.5 to 16 nm size regime, which is typically employed in most catalytic studies. The nanoparticles mostly have spherical shape, however octahedron type particles can also be observed in samples with larger nanoparticles.

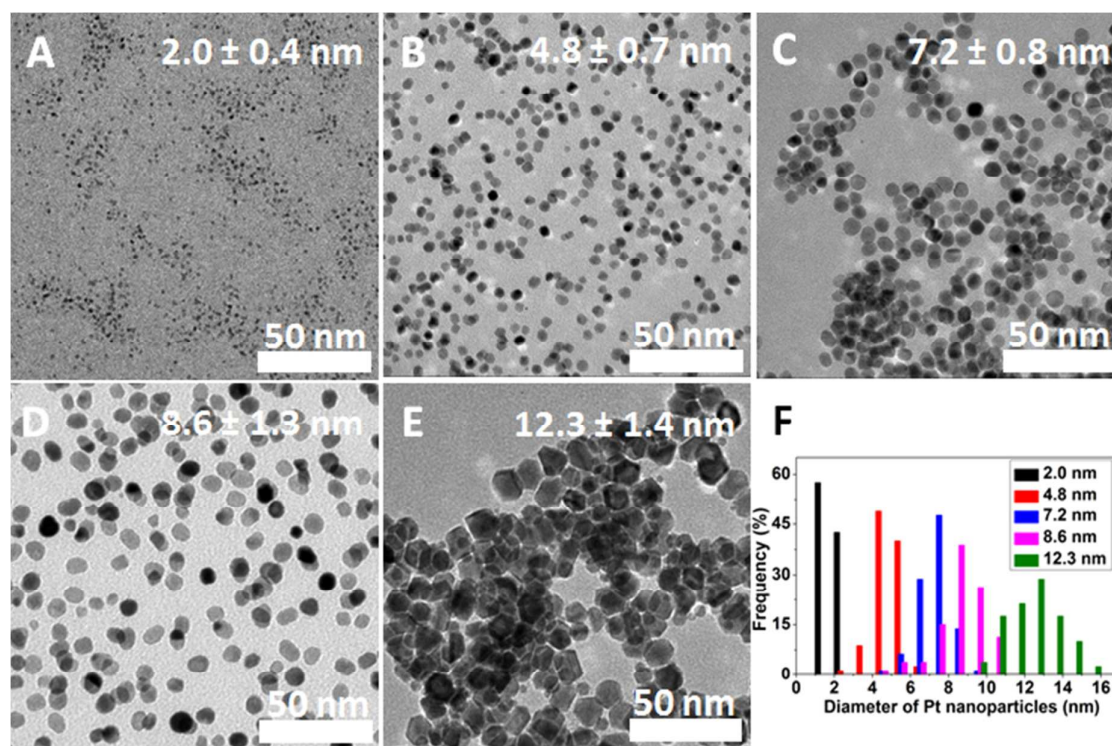


**Figure 5** TEM images of the different sized Pt nanoparticles (A-E), together with the comparison of their size distributions (F).

To investigate the morphology of the Pt/NiO electrodes SEM and TEM images were recorded. SEM image of a Pt/NiO electrode (7.2 nm average Pt diameter) is compared to the corresponding bare NiO in Figure 6. Even at high magnifications, the 7.2 nm Pt nanoparticles are too small to be observed directly, however there are some distinguishable changes, which indicate the presence of Pt on the NiO surface. First, the surface is smoother before drop-casting of Pt, than afterwards. Furthermore, upon drop-casting, the pore structure also altered: the diameter of the pores decreased and some were even clogged. The pore size distribution was also determined before and after decoration with Pt (Figure 6C). Most importantly, the fraction of the large pores decreased notably, due to the incorporation of Pt nanoparticles. The amount of the small pores increased in parallel as expected. These observations together indicate that a high amount of Pt nanoparticles accumulated in the pores, close to the top of the NiO layer.

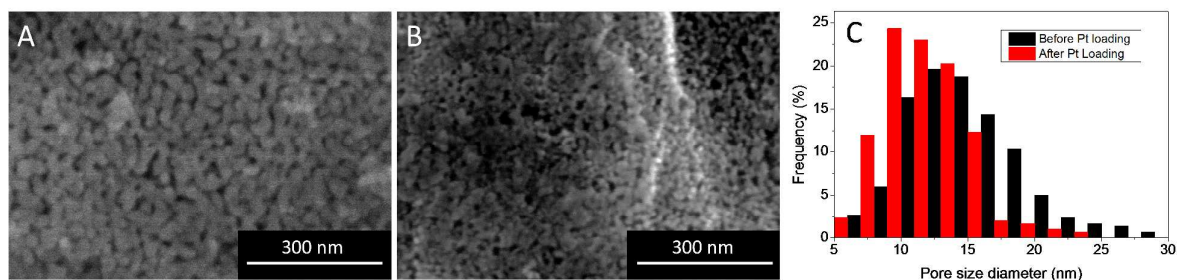


**Figure 6.** SEM images of **A:** an anodized NiO film, **B:** a Pt/NiO composite (7.2 nm Pt). **C:** pore size distribution before and after anchoring Pt (determined from SEM images in A and B).

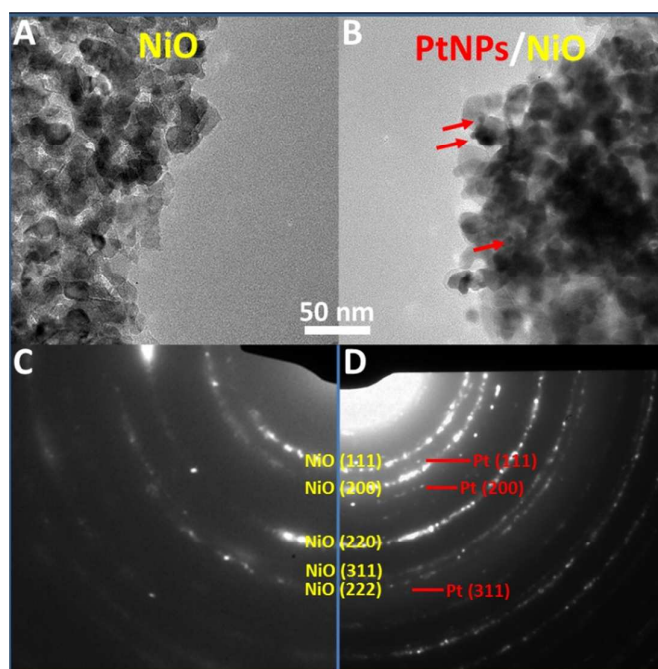


**Figure 7.** **A:** Typical TEM images of a heat treated porous NiO and **B:** a Pt/NiO sample containing 7.2 nm average diameter Pt nanoparticles with a surface concentration of 5  $\mu\text{g}/\text{cm}^2$ . **C, D:** electron diffraction patterns of the respective materials shown in A and B.

TEM images of the debris of porous NiO films were scrutinized, and the presence of a mesoporous structure was witnessed. The average diameter of the joined building blocks were around 20 nm (Figure 7A). Note that this value is in perfect agreement with the previously shown XRD and SEM data. As for the Pt/NiO sample (containing 7.2 nm Pt), individual Pt nanoparticles can be spotted on the image (Figure 7B). The electron diffraction study of the nanoporous nickel oxide reveals NiO (111), Ni (200), NiO (200), NiO (220), NiO (311) and NiO (222) crystallite planes characteristic for face-centered cubic (*fcc*) nickel(II) oxide

(Figure 7C.). For Pt-decorated NiO, crystallite planes of Pt (111), Pt (200) and Pt (311) showed the presence of metallic face-centered cubic (*fcc*) platinum (Figure 7D).

HR-TEM images were also recorded for a composite sample with higher Pt loading ( $10 \mu\text{g cm}^{-2}$ , Figure 8 and Figure S6). The most important message of this TEM images is that nanosized Pt particles can be spotted anchored to the interconnected porous structure of NiO. In addition, clear lattice fringes corresponding to the (111) facets of Pt as well as the (111) facets of NiO were observed (Fig. 8).

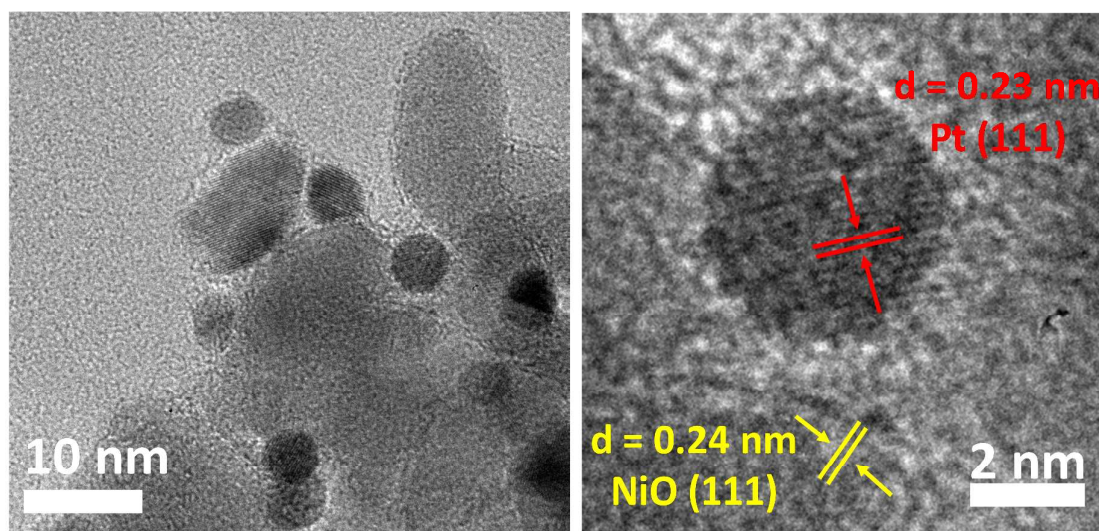


**Figure 8.** High-Resolution TEM images of 7.2 nm Pt nanoparticles anchored onto the surface of nanoporous NiO.

### XPS measurements

To evaluate the surface chemical characteristics of the NiO electrodes and the drop-casted Pt nanoparticles, XPS measurements were carried out. NiO-based materials exhibit complex surface chemistry because of non-stoichiometry and hydration under ambient conditions.<sup>46</sup> The presence of different Ni-oxide/hydroxide species can make the quantitative evaluation of the XP spectra problematic and should be only attempted in the presence of high quality standards.<sup>46-48</sup> In this vein, we focused on the qualitative evaluation of the surface characteristics. In Figure 9 regions corresponding to Ni 3p (A), Ni 2p (B) and O 1s (C) are

shown for a NiO sample decorated with 8.6 nm average diameter Pt nanoparticles. Because of the extensive overlap between the Ni 3p and the Pt 4f signals, deconvolution of the Ni 3p components was not attempted. Judging from the position of the asymmetric Pt 4f<sub>7/2</sub> component (71.2 eV), together with the Pt 4d<sub>5/2</sub> peak positions (Figure S8) however, the zero valence of the drop-casted Pt can be confirmed in all cases (Figure 9A).<sup>49,50</sup> Notably, a small amount of surface oxide (PtO) was only detected in the case of the smallest Pt nanoparticles (Figure S8). The main Ni 2p<sub>3/2</sub> line was modeled with three components: (i) NiO (853.7 eV), (ii) Ni(OH)<sub>2</sub> (855.2 eV) and NiOOH (856.4 eV) which are consistent with literature data.<sup>46</sup> The addition of NiOOH into the model was dictated by the chemical nature of the samples, because its formation is characteristic of electrochemically grown NiO layers.<sup>24,51</sup> In the O 1s region (Figure 9C) similar chemical entities were distinguished in accordance with previous literature data.<sup>46</sup> When fitting the spectrum the contribution from oxygens of NiO (529.2 eV), Ni(OH)<sub>2</sub> (530.7 eV), NiOOH (532.1 eV), and physisorbed H<sub>2</sub>O (532.9 eV) were all taken into account.

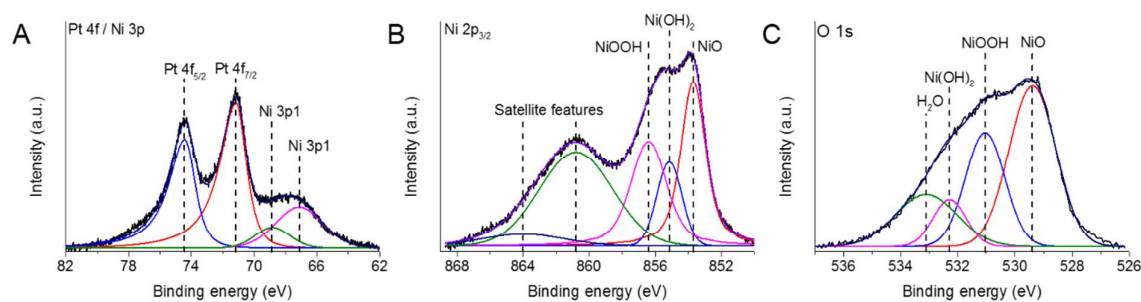
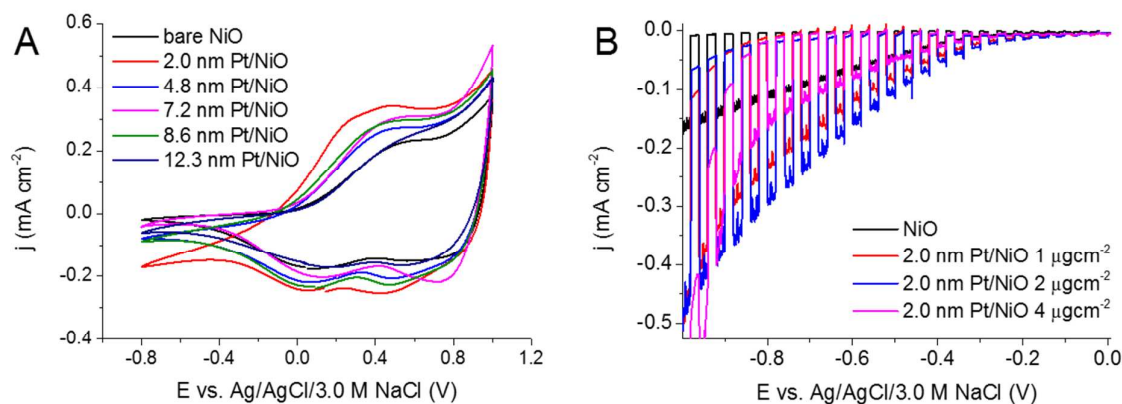


**Figure 9.** **A:** Pt 4f / Ni 3p XP spectrum, **B:** Ni 2p<sub>3/2</sub> XP spectrum, **C:** and O 1s XP spectrum of the NiO sample decorated with 8.6 nm Pt nanoparticles. Resolved curves are added only to guide the eye to changes in spectral shape and do not represent sufficient component analysis.

### Electrochemical and photoelectrochemical characterization

To assess the dark electrochemical behavior of the Pt/NiO nanocomposites, cyclic voltammograms (CVs) were recorded (Figure 10A). Two main trends were immediately observed upon the addition of Pt: (i) a dark current developed in the range of  $E = -1.0$  V -  $-0.4$  V (arising from direct water reduction on the Pt nanoparticles) and (ii) a change in the overall

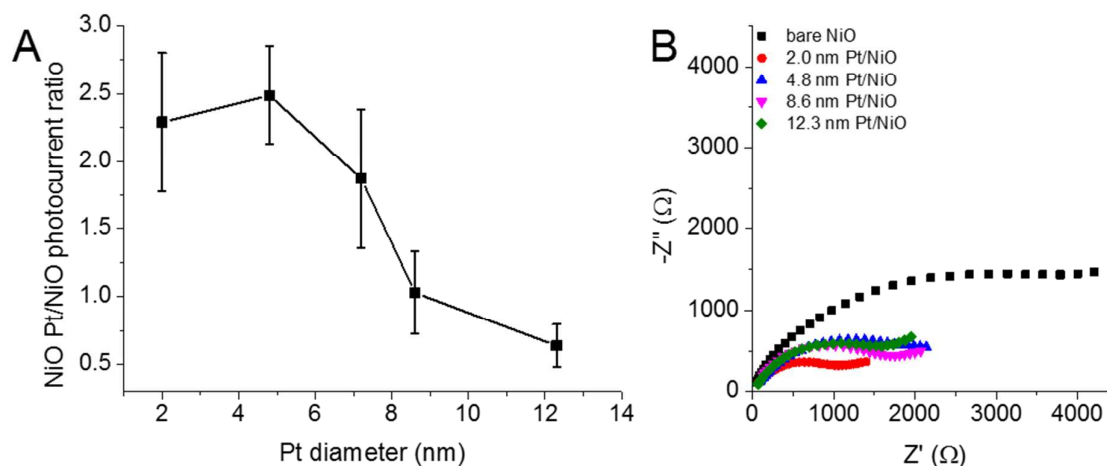
1  
2  
3 electroactivity of the electrodes. For pristine NiO, negligible dark current flow was observed  
4  
5 at the cathodic end of the potential window ( $E = -1.0$  V -  $-0.4$  V). When the surface of the NiO  
6  
7 electrodes is decorated with Pt nanoparticles, however the gradual evolution of a dark current  
8  
9 was witnessed. The onset potential of this process is located at  $E = -0.2$  V regardless of the  
10  
11 size of the Pt nanoparticles. This observation indicates that the size of the nanoparticles  
12  
13 predominantly affects the kinetic aspects of the dark water reduction process. In the positive  
14  
15 potential regime ( $E > 0.0$  V) higher electrochemical activity was observed for the Pt loaded  
16  
17 NiO samples compared to their pristine NiO counterpart. Although the electrochemical  
18  
19 transformation of NiO and Pt overlap in this potential regime, the increased electroactivity  
20  
21 can be attributed to the presence of Pt related redox peaks.<sup>31,52</sup> Among all the studied samples  
22  
23 the one decorated with 2.0 nm Pt nanoparticles exhibited the highest electrochemical activity,  
24  
25 and the relative enhancement decreased with the increasing Pt particle size. These data served  
26  
27 as the basis of normalization of the PEC performance (see below), where the actual surface  
28  
29 area of the co-catalyst may play a key role in the overall performance.  
30  
31  
32  
33



34  
35  
36  
37  
38  
39  
40  
41  
42  
43  
44  
45  
46  
47 **Figure 10. A:** Cyclic voltammograms of NiO and Pt/NiO composites  $2 \mu\text{g cm}^{-2}$ . **B:** Linear  
48  
49 photovoltammogram of Pt/NiO 2.0 nm, with different Pt loading in 0.2 M  $\text{Na}_2\text{SO}_4$ , saturated  
50  
51 with  $\text{N}_2$  gas.

52  
53 To characterize the PEC behavior of the Pt/NiO composites, linear sweep  
54  
55 photovoltammetry measurements were carried out with a slow sweep rate ( $2 \text{ mV s}^{-1}$ ) in 0.2 M  
56  
57  $\text{Na}_2\text{SO}_4$ . The illumination was periodically interrupted (0.1 Hz) to record the response of the  
58  
59  
60

1  
2  
3 electrodes under both dark and illuminated conditions. In almost all the cases (except for the  
4  
5 largest Pt size), the cathodic photocurrents of the Pt-decorated NiO samples surpassed their  
6  
7 pristine NiO counterparts. This superior behavior could be attributed to the more efficient  
8  
9 electron-hole separation in the prepared nanocomposites.<sup>23</sup> By increasing the Pt loading,  
10  
11 higher photocurrents were achieved until an optimal composition was reached. After this  
12  
13 maximum, the optical shielding effect of the Pt nanoparticles on the surface resulted in a  
14  
15 decrease in the photocurrents. For the largest particle this shielding effect seemed to be  
16  
17 deleterious even at moderate loadings. To strip the measured photocurrent enhancements from  
18  
19 possible uncertainty arising from the use of different NiO electrodes, the photocurrents were  
20  
21 normalized by the photocurrent measured for the respective pristine NiO electrodes (Figure  
22  
23 S7). To find the optimal composition and particle size, these normalized photocurrent values  
24  
25 were determined of each Pt decorated sample (Figure 11A, and Figure S7). It is apparent that  
26  
27 the largest increase in the photocurrent value was achieved in the case of 2.0 nm and 4.8 nm  
28  
29 sized Pt nanoparticles.  
30  
31  
32  
33



34  
35  
36  
37  
38  
39  
40  
41  
42  
43  
44  
45  
46  
47  
48  
49  
50  
51  
52  
53  
54  
55  
56  
57  
58  
59  
60

**Figure 11. A:** Particle size dependence of the photocurrent enhancement for the Pt/NiO samples ( $2 \mu\text{g cm}^{-2}$  loading). The error bar represents measurements carried out for three different sample for each particle size. Lines connecting the measured data serve as guides for the eye only. **B:** Nyquist plots of the electrochemical impedance spectroscopy data, recorded for the bare and different Pt-decorated samples, at  $E = 0.0\text{V}$  in the 10 Hz to 0.1 MHz frequency range, in 1.0 M  $\text{Na}_2\text{SO}_4$  solution. The inset shows the magnified region of the semicircles.

1  
2  
3 The origin of this photocurrent enhancement however, is complex and convoluted.  
4  
5 First of all, the surface area difference of the various sized Pt nanoparticles can be reflected in  
6  
7 these increased values. To exclude this factor and to shed light on possible other, more  
8  
9 sophisticated size-effects, further normalization of the data was carried out. The extra redox  
10  
11 peak observed for the Pt-decorated samples during CV measurements is a direct indicator of  
12  
13 the electroactive surface area of the Pt nanoparticles. As the first step, the charge capacitance  
14  
15 of the bare NiO was subtracted from that of the Pt-decorated samples. Subsequently, the  
16  
17 normalization of the photocurrent enhancement with respect of the electrochemically active  
18  
19 surface area of the Pt nanoparticles was carried out. When the trivial surface area effect was  
20  
21 stripped from the data the maximum photocurrent increase was obtained for the samples  
22  
23 decorated with 4.8 nm and 7.2 nm sized Pt nanoparticles.  
24  
25  
26

27 This observation is indeed interesting, because in earlier studies the highest  
28  
29 heterogeneous/electro-catalytic activity was typically observed for even smaller particles  
30  
31 (mostly because of the larger number of active sites).<sup>30-35</sup> In our case however, the  
32  
33 compatibility of the NiO and Pt has to be also considered. As the average pore size of the  
34  
35 optimized NiO samples was  $15\pm 5$  nanometers (see also pore size distribution in Figure 1C),  
36  
37 the large sized Pt particles simply don't infiltrate into the deeper regions of the nanoporous  
38  
39 NiO film, but rather remain on its top. Such architecture is obviously not favorable  
40  
41 considering the low contact area between NiO and Pt, and the possible optical shielding  
42  
43 effect. On the other hand, the smallest (2 nm) Pt particles are likely to penetrate to the bottom  
44  
45 region of the anodized NiO layer. As the light penetration is limited in the deeper regions, the  
46  
47 co-catalytic effect of these deeply embedded Pt particles cannot be fully harnessed. Finally,  
48  
49 the intermediate sized (4.8 nm and 7.2 nm) Pt particles may partially penetrate, resulting in a  
50  
51 beneficial Pt/NiO nanoarchitectures. This hypothesis is qualitatively supported by XPS data,  
52  
53 where the surface concentration of the Pt nanoparticles was estimated. It was found that the  
54  
55  
56  
57  
58  
59  
60

1  
2  
3 high specific surface area of the small sized Pt nanoparticles is not reflected in the surface  
4  
5 Pt/Ni ratio, most likely because it is compensated by their increased penetration into the NiO  
6  
7 layer (where they are invisible for XPS).  
8

9  
10 Electrochemical Impedance Spectroscopy (EIS) measurements were carried out to  
11  
12 characterize the electrical properties of the Pt decorated NiO electrodes. The Nyquist-plots of  
13  
14 the samples are presented in Figure 11B. Qualitatively, one may notice that the impedance  
15  
16 spectra exhibit a depressed semicircle at high frequencies. It is also apparent that all Pt  
17  
18 containing samples possess lower charge transfer resistance (the decrease in the endpoint of  
19  
20 the semicircle) compared to the bare NiO electrodes. Overall, the lowest charge transfer  
21  
22 resistance was obtained for the sample with the smallest Pt size, but all Pt-decorated  
23  
24 electrodes have much smaller  $R_{ct}$ , compared to the bare NiO. This trend suggest that the  
25  
26 photocurrent increase is rooted in the improved charge transfer at the electrode/electrolyte  
27  
28 interface. Further details, including the fitting of EIS data and the employed equivalent circuit  
29  
30 are shown in the Supporting Information (Figure S10 and Figure S11).  
31  
32  
33

34 To further study the origin of the photocurrent enhancement, photoaction spectra were  
35  
36 recorded. Figure S9 shows the photoaction spectra of the pristine and 2.0 nm sized Pt  
37  
38 decorated NiO electrodes in 0.2 M  $\text{Na}_2\text{SO}_4$  recorded at a constant bias potential of  $E = -0.8\text{V}$ .  
39  
40 The bandgap of the materials was estimated by fitting the cut-off region of the photoaction  
41  
42 spectra with a straight line segment and extrapolating it to the wavelength axis. For both the  
43  
44 pristine and Pt decorated samples a similar bandgap value of  $E_{bg} = 3.55\text{ eV}$  was found. This is  
45  
46 in good agreement with the 3.5 eV value reported for NiO in the literature,<sup>23</sup> and our own  
47  
48 optical data obtained via diffuse reflectance UV-Vis spectroscopy ( $3.50 \pm 0.1\text{ eV}$ , raw data  
49  
50 not shown here). The decoration of the NiO electrodes with Pt nanoparticles leaves the  
51  
52 bandgap of the oxide hybrids intact. Therefore, confirming our previous conclusion, the  
53  
54  
55  
56  
57  
58  
59  
60

improvement in the PEC behavior of the Pt decorated samples can be attributed to better charge separation rather than increased optical absorption.

### Long-term photoelectrochemical measurements

Long term photoelectrolysis, combined with in-situ gas phase analysis, was performed to monitor the formation of H<sub>2</sub> gas (Figure 12). At the initial stage of the photoelectrolysis some dark current was detected, most likely because of the reduction of some minority Ni(III) species in the sample (see also XPS data above). The measured photocurrents slowly decreased during the electrolysis, partly because of the leaching of Pt nanoparticles to the solution (as confirmed by comparing the XPS data before and after photoelectrolysis). After half an hour, there was a detectable amount of H<sub>2</sub> in the gas phase. The H<sub>2</sub> concentration increased linearly with the transferred charge. The Faradaic efficiency of this process was around 70%, most likely because of minor leaking of the electrochemical cell. Long-term measurements for other Pt/ NiO electrodes (with different Pt sizes) were also conducted (not shown here), where a similar pattern was found. XPS investigations taken after the long-term measurements revealed that the chemical state of Pt and NiO was not altered during the process.

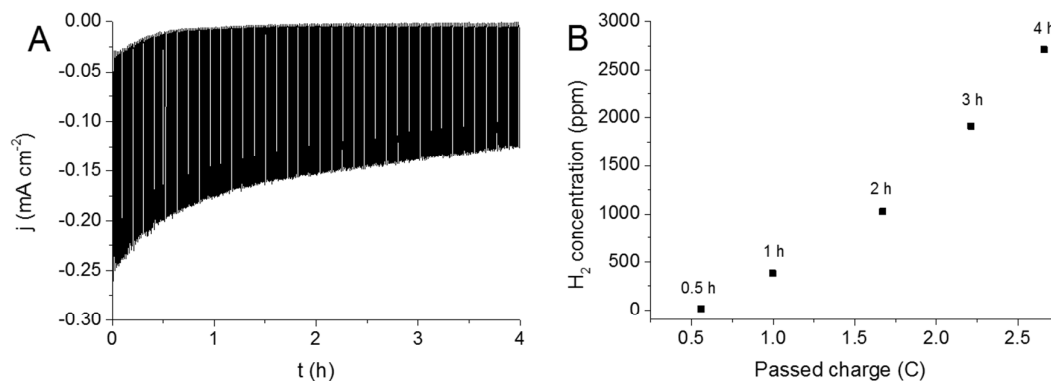


**Figure 12.** **A:** Long-term photoelectrolysis on a Pt/NiO electrode (7.2 nm sized Pt) at E= -0.8 V potential in 0.2 M Na<sub>2</sub>SO<sub>4</sub>. **B:** The amount of evolved H<sub>2</sub> during the long-term measurement shown in A.

### Conclusions

1  
2  
3 In this study, we carried out the simultaneous optimization of nanoporous NiO and Pt  
4 nanoparticles to assemble Pt/NiO composite photoelectrodes with improved PEC  
5 performance. This system served as a *model* for photoelectrodes encompassing a  
6 semiconductor light absorber and a metal nanoparticle co-catalyst. As the first step a new  
7 anodization protocol was developed, which allowed the formation of pure NiO, with  
8 controlled morphological attributes. In the second step, Pt nanoparticles were synthesized  
9 with precise size control (5 sizes between 2.0 and 12.3 nm average diameter) and narrow size  
10 distribution. Finally, the Pt nanoparticles were anchored on the NiO surface with different  
11 loadings. All the hybrid samples showed enhanced cathodic photocurrents compared to the  
12 bare NiO film, although to notably different extents. It was shown that the enhanced PEC  
13 activity is rooted in the lower charge carrier recombination rate in the case of the composite  
14 samples (i.e., Pt acted as a co-catalyst in the H<sub>2</sub> evolution reaction). Comparing the relative  
15 enhancements in the photocurrents upon the addition of different sized Pt particles, it was  
16 found that the two smallest (2.0 and 4.8 nm) have the most beneficial effect. After peeling off  
17 the trivial surface area effect (performed by normalizing the photocurrent enhancement with  
18 the electrochemically active surface area of Pt) the two intermediate particle sizes (4.8 and 7.2  
19 nm) were found to be significantly better than both the smaller and larger particles. The main  
20 outcome of this study is that the size of the co-catalyst exert an important role in the overall  
21 performance, similarly to the electrocatalytic and photocatalytic scenarios.<sup>30–35</sup> The complete  
22 picture however, is even more complicated because light absorption, charge carrier transport,  
23 and surface chemical reactions have to be considered at the same time. We have demonstrated  
24 that in the case of nanocomposite photoelectrodes (e.g., light absorber + co-catalyst) the  
25 nanoscale structure of the components has to be optimized simultaneously, to achieve  
26 reasonable PEC activity. The conclusions of this study may lead to new design concepts of  
27 photoelectrode assemblies, and such endeavors are in progress in our laboratories.  
28  
29  
30  
31  
32  
33  
34  
35  
36  
37  
38  
39  
40  
41  
42  
43  
44  
45  
46  
47  
48  
49  
50  
51  
52  
53  
54  
55  
56  
57  
58  
59  
60

## Acknowledgements

The authors thank Dr. Tamás Pajkossy (Research Center for Natural Sciences of the Hungarian Academy of Sciences) for the valuable discussions on the EIS results. The authors are very thankful to Prof. Frank Osterloh (University of California, Davis) for his constructive criticism and insightful comments on an earlier version of this manuscript. Authors are grateful for Ildikó Kálmista and Prof. Gábor Galbács for ICP-MS measurements. The authors thank the assistance of the colleagues at Rendernet Ltd., provided in the preparation of the artwork. This project has received funding from the European Research Council (ERC) under the European Union's Horizon 2020 research and innovation programme (grant agreement No 716539). This collaborative research was partially supported by the "Széchenyi 2020" program in the framework of GINOP-2.3.2-15-2016-00013 "Intelligent materials based on functional surfaces – from syntheses to applications" project and the Hungarian National Research Development and Innovation Office through projects K K 112531, K 120115, and PD 120877. This paper was also supported by the János Bolyai Research Scholarship of the Hungarian Academy of Sciences and the ÚNKP-ÚNKP-16-4 New National Excellence Program of the Ministry of Human Capacities (A. S.).

## Supporting Information Available

Additional SEM images, EDX spectra, description of Pt nanoparticle synthesis, TEM images, PEC data, XP spectra, Photoaction spectra, electrochemical impedance spectra. This information is available free of charge via the Internet at <http://pubs.acs.org>.

## References

- (1) Lewis, N.; Nocera, D. Powering the Planet: Chemical Challenges in Solar Energy Utilization. *Proc. Natl. Acad. Sci.* **2006**, *104*, 15729–15735.
- (2) Lewis, N. S. Research Opportunities to Advance Solar Energy Utilization. *Science* **2016**, *351*, 353–362.

- 1  
2  
3 (3) Chen, Z.; Jaramillo, T. F.; Deutsch, T. G.; Kleiman-Shwarscstein, A.; Forman, A. J.;  
4 Gaillard, N.; Garland, R.; Takane, K.; Heske, C.; Sunkara, M.; et al. Accelerating  
5 Materials Development for Photoelectrochemical Hydrogen Production: Standards for  
6 Methods, Definitions, and Reporting Protocols. *J. Mater. Res.* **2010**, *25*, 3–16.  
7  
8  
9  
10  
11 (4) Rajeshwar, K. Hydrogen Generation at Irradiated Oxide Semiconductor–solution  
12 Interfaces. *J. Appl. Electrochem.* **2007**, *37*, 765–787.  
13  
14  
15  
16 (5) Rajeshwar, K. Solar Energy Conversion and Environmental Remediation Using  
17 Inorganic Semiconductor–Liquid Interfaces: The Road Traveled and the Way Forward.  
18 *J. Phys. Chem. Lett.* **2011**, *2*, 1301–1309.  
19  
20  
21  
22  
23 (6) Krol, R. van de. Principles of Photoelectrochemical Cells. In *Photoelectrochemical*  
24 *Hydrogen Production*; Krol, R. van de, Gratzel, M., Eds.; Springer, 2012; Vol. 102, pp  
25 13–67.  
26  
27  
28  
29  
30 (7) Khaselev, O.; Turner, J. A. A Monolithic Photovoltaic-Photoelectrochemical Device  
31 for Hydrogen Production via Water Splitting. *Science* **1998**, *280*, 425–427.  
32  
33  
34 (8) Sun, K.; Liu, R.; Chen, Y.; Verlage, E.; Lewis, N. S.; Xiang, C. A Stabilized,  
35 Intrinsically Safe, 10% Efficient, Solar-Driven Water-Splitting Cell Incorporating  
36 Earth-Abundant Electrocatalysts with Steady-State pH Gradients and Product  
37 Separation Enabled by a Bipolar Membrane. *Adv. Energy Mater.* **2016**, *6*, 1600379.  
38  
39  
40  
41  
42 (9) Kamat, P. V.; Christians, J. A. Solar Cells versus Solar Fuels: Two Different  
43 Outcomes. *J. Phys. Chem. Lett.* **2015**, *6*, 1917–1918.  
44  
45  
46  
47 (10) Osterloh, F. E. Inorganic Nanostructures for Photoelectrochemical and Photocatalytic  
48 Water Splitting. *Chem. Soc. Rev.* **2013**, *42*, 2294–2320.  
49  
50  
51  
52 (11) Sivula, K.; van de Krol, R. Semiconducting Materials for Photoelectrochemical Energy  
53 Conversion. *Nat. Rev. Mater.* **2016**, *1*, 15010.  
54  
55  
56 (12) Bang, J. H.; Kamat, P. V. Solar Cells by Design: Photoelectrochemistry of TiO<sub>2</sub>  
57  
58  
59  
60

- 1  
2  
3 Nanorod Arrays Decorated with CdSe. *Adv. Funct. Mater.* **2010**, *20*, 1970–1976.
- 4  
5 (13) Liu, N.; Lee, K.; Schmuki, P. Small Diameter TiO<sub>2</sub> Nanotubes vs. Nanopores in Dye  
6  
7 Sensitized Solar Cells. *Electrochem. Commun.* **2012**, *15*, 1–4.
- 8  
9 (14) Janáky, C.; Chanmanee, W.; Rajeshwar, K. On the Substantially Improved  
10  
11 Photoelectrochemical Properties of Nanoporous WO<sub>3</sub> Through Surface Decoration  
12  
13 with RuO<sub>2</sub>. *Electrocatalysis* **2013**, *4*, 382–389.
- 14  
15 (15) Bignozzi, C. A.; Caramori, S.; Cristino, V.; Argazzi, R.; Meda, L.; Tacca, A.  
16  
17 Nanostructured Photoelectrodes Based on WO<sub>3</sub>: Applications to Photooxidation of  
18  
19 Aqueous Electrolytes. *Chem. Soc. Rev.* **2013**, *42*, 2228–2246.
- 20  
21 (16) Hu, L.; Peng, J.; Wang, W.; Xia, Z.; Yuan, J.; Lu, J.; Huang, X.; Ma, W.; Song, H.;  
22  
23 Chen, W.; et al. Sequential Deposition of CH<sub>3</sub>NH<sub>3</sub>PbI<sub>3</sub> on Planar NiO Film for  
24  
25 Efficient Planar Perovskite Solar Cells. *ACS Photonics* **2014**, *1*, 547–553.
- 26  
27 (17) Nattestad, A.; Mozer, A. J.; Fischer, M. K. R.; Cheng, Y.; Mishra, A.; Bäuerle, P.;  
28  
29 Bach, U. Efficient Photocathodes for Dye-Sensitized Tandem Solar Cells. *Nat. Mater.*  
30  
31 **2010**, *9*, 31–35.
- 32  
33 (18) Li, L.; Gibson, E. A.; Qin, P.; Boschloo, G.; Gorlov, M.; Hagfeldt, A.; Sun, L. Double-  
34  
35 Layered NiO Photocathodes for P-Type DSSCs with Record IPCE. *Adv. Mater.* **2010**,  
36  
37 *22*, 1759–1762.
- 38  
39 (19) Dare-edwards, M. P.; Goodenough, J.; Hamnett, A.; Nicholson, N. D.  
40  
41 Photoelectrochemistry of Nickel (II) Oxide. *J. Chem. Soc., Faraday Trans.* **1981**, *77*,  
42  
43 643–661.
- 44  
45 (20) Lin, C.-Y.; Lai, Y.-H.; Mersch, D.; Reisner, E. Cu<sub>2</sub>O|NiO<sub>x</sub> Nanocomposite as an  
46  
47 Inexpensive Photocathode in Photoelectrochemical Water Splitting. *Thin Solid Films*  
48  
49 **2014**, *8*, 252–257.
- 50  
51 (21) Gross, M. A.; Creissen, C. E.; Orchard, K. L.; Reisner, E. Photoelectrochemical  
52  
53  
54  
55  
56  
57  
58  
59  
60

- 1  
2  
3 Hydrogen Production in Water Using a Layer-by-Layer Assembly of a Ru Dye and Ni  
4 Catalyst on NiO. *Chem. Sci.* **2016**, *7*, 242–247.
- 5  
6  
7 (22) Sahara, G.; Abe, R.; Higashi, M.; Morikawa, T.; Maeda, K.; Ueda, Y.; Ishitani, O.  
8  
9 Photoelectrochemical CO<sub>2</sub> Reduction Using a Ru(II)-Re(I) Multinuclear Metal  
10 Complex on a P-Type Semiconducting NiO Electrode. *Chem. Commun.* **2015**, *51*,  
11 10722–10725.  
12  
13  
14  
15  
16 (23) Nail, B. A.; Fields, J. M.; Zhao, J.; Wang, J.; Greaney, M. J.; Brutchey, R. L.; Osterloh,  
17  
18 F. E. Nickel Oxide Particles Catalyze Photochemical Hydrogen Evolution from  
19 Water—Nanoscaling Promotes P-Type Character and Minority Carrier Extraction. *ACS*  
20 *Nano* **2015**, *9*, 5135–5142.  
21  
22  
23  
24  
25 (24) Hu, C.; Chu, K.; Zhao, Y.; Teoh, W. Y. Efficient Photoelectrochemical Water Splitting  
26 over Anodized P -Type NiO Porous Films. *ACS Appl. Mater. Interfaces* **2014**, *6*,  
27 18558–18568.  
28  
29  
30  
31  
32 (25) Sun, K.; McDowell, M. T.; Nielander, A. C.; Hu, S.; Shaner, M. R.; Yang, F.;  
33  
34 Brunshwig, B. S.; Lewis, N. S. Stable Solar-Driven Water Oxidation to O<sub>2</sub>(g) by Ni-  
35 Oxide-Coated Silicon Photoanodes. *J. Phys. Chem. Lett.* **2015**, *6*, 592–598.  
36  
37  
38  
39 (26) Kenney, M. J.; Gong, M.; Li, Y.; Wu, J. Z.; Feng, J.; Lanza, M.; Dai, H. High-  
40 Performance Silicon Photoanodes Passivated with Ultrathin Nickel Films for Water  
41 Oxidation. *Science* **2013**, *342*, 836–840.  
42  
43  
44  
45 (27) Subramanian, V.; Wolf, E. E.; Kamat, P. V. Catalysis with TiO<sub>2</sub> /Gold  
46 Nanocomposites. Effect of Metal Particle Size on the Fermi Level Equilibration. *J. Am.*  
47 *Chem. Soc.* **2004**, *126*, 4943–4950.  
48  
49  
50  
51 (28) Subramanian, V.; Wolf, E.; Kamat, P. V. Semiconductor - Metal Composite  
52 Nanostructures. To What Extent Do Metal Nanoparticles Improve the Photocatalytic  
53 Activity of TiO<sub>2</sub> Films? *J. Phys. Chem. B* **2001**, *105*, 11439–11446.  
54  
55  
56  
57  
58  
59  
60

- 1  
2  
3 (29) McCrory, C. C. L.; Jung, S.; Ferrer, I. M.; Chatman, S. M.; Peters, J. C.; Jaramillo, T.  
4  
5 F. Benchmarking Hydrogen Evolving Reaction and Oxygen Evolving Reaction  
6  
7 Electrocatalysts for Solar Water Splitting Devices. *J. Am. Chem. Soc.* **2015**, *137*, 4347–  
8  
9 4357.  
10  
11 (30) Shao, M.; Peles, A.; Shoemaker, K. Electrocatalysis on Platinum Nanoparticles :  
12  
13 Particle Size Effect on Oxygen Reduction Reaction Activity. *Nano Lett.* **2011**, *11*,  
14  
15 3714–3719.  
16  
17 (31) Arenz, M.; Mayrhofer, K. J. J.; Stamenkovic, V.; Blizanac, B. B.; Tomoyuki, T.; Ross,  
18  
19 P. N.; Markovic, N. M. The Effect of the Particle Size on the Kinetics of CO  
20  
21 Electrooxidation on High Surface Area Pt Catalysts. *J. Am. Chem. Soc.* **2005**, *127*,  
22  
23 6819–6829.  
24  
25 (32) Sapi, A.; Liu, F.; Cai, X.; Thompson, C. M.; Wang, H.; An, K.; Krier, J. M.; Somorjai,  
26  
27 G. A. Comparing the Catalytic Oxidation of Ethanol at the Solid–Gas and Solid–Liquid  
28  
29 Interfaces over Size-Controlled Pt Nanoparticles: Striking Differences in Kinetics and  
30  
31 Mechanism. *Nano Lett.* **2014**, *14*, 6727–6730.  
32  
33 (33) Wang, H.; Wang, Y.; Zhu, Z.; Sapi, A.; An, K.; Kennedy, G.; Michalak, W. D.;  
34  
35 Somorjai, G. A. Influence of Size-Induced Oxidation State of Platinum Nanoparticles  
36  
37 on Selectivity and Activity in Catalytic Methanol Oxidation in the Gas Phase. *Nano*  
38  
39 *Lett.* **2013**, *13*, 2976–2979.  
40  
41 (34) Wang, H.; Sapi, A.; Thompson, C. M.; Liu, F.; Zherebetsky, D.; Krier, J. M.; Carl, L.  
42  
43 M.; Cai, X.; Wang, L.-W.; Somorjai, G. A. Dramatically Different Kinetics and  
44  
45 Mechanism at Solid/Liquid and Solid/Gas Interfaces for Catalytic Isopropanol  
46  
47 Oxidation over Size-Controlled Platinum Nanoparticles. *J. Am. Chem. Soc.* **2014**, *136*,  
48  
49 10515–10520.  
50  
51 (35) Pushkarev, V. V.; An, K.; Alayoglu, S.; Beaumont, S. K.; Somorjai, G. A.  
52  
53  
54  
55  
56  
57  
58  
59  
60

- 1  
2  
3 Hydrogenation of Benzene and Toluene over Size Controlled Pt/SBA-15 Catalysts:  
4 Elucidation of the Pt Particle Size Effect on Reaction Kinetics. *J. Catal.* **2012**, *292*, 64–  
5 72.  
6  
7  
8  
9  
10 (36) Kmetykó, Á.; Mogyorósi, K.; Gerse, V.; Kónya, Z.; Pusztai, P.; Dombi, A.; Hernádi,  
11 K. Photocatalytic H<sub>2</sub> Production Using Pt-TiO<sub>2</sub> in the Presence of Oxalic Acid:  
12 Influence of the Noble Metal Size and the Carrier Gas Flow Rate. *Materials* **2014**, *7*,  
13 7022–7038.  
14  
15  
16  
17  
18 (37) Wang, W.; An, W.; Ramalingam, B.; Mukherjee, S.; Niedzwiedzki, D. M.;  
19 Gangopadhyay, S.; Biswas, P. Size and Structure Matter: Enhanced CO<sub>2</sub>  
20 Photoreduction Efficiency by Size-Resolved Ultrafine Pt Nanoparticles on TiO<sub>2</sub> Single  
21 Crystals. *J. Am. Chem. Soc.* **2012**, *134*, 11276–11281.  
22  
23  
24  
25  
26  
27 (38) Lombardi, I.; Marchionna, S.; Zangari, G.; Pizzini, S. Effect of Pt Particle Size and  
28 Distribution on Photoelectrochemical Hydrogen Evolution by P-Si Photocathodes.  
29 *Langmuir* **2007**, *23*, 12413–12420.  
30  
31  
32  
33  
34 (39) Shrestha, N. K.; Yang, M.; Schmuki, P. Self-Ordered Nanoporous Nickel  
35 Oxide/Fluoride Composite Film with Strong Electrochromic Contrast. *Electrochem.*  
36 *Solid-State Lett.* **2010**, *13*, C21-C24.  
37  
38  
39  
40 (40) Roy, P.; Berger, S.; Schmuki, P. TiO<sub>2</sub> Nanotubes: Synthesis and Applications. *Angew.*  
41 *Chemie Int. Ed.* **2011**, *50*, 2904–2939.  
42  
43  
44  
45 (41) Samu, G. F.; Pencz, K.; Janáky, C.; Rajeshwar, K. On the Electrochemical Synthesis  
46 and Charge Storage Properties of WO<sub>3</sub>/polyaniline Hybrid Nanostructures. *J. Solid*  
47 *State Electrochem.* **2015**, *19*, 2741–2751.  
48  
49  
50  
51 (42) Macak, J. M.; Hildebrand, H.; Marten-Jahns, U.; Schmuki, P. Mechanistic Aspects and  
52 Growth of Large Diameter Self-Organized TiO<sub>2</sub> Nanotubes. *J. Electroanal. Chem.*  
53 **2008**, *621*, 254–266.  
54  
55  
56  
57  
58  
59  
60

- 1  
2  
3 (43) Zhou, G.; Wang, D.-W.; Yin, L.-C.; Li, N.; Li, F.; Cheng, H.-M. Oxygen Bridges  
4 between NiO Nanosheets and Graphene for Improvement of Lithium Storage. *ACS*  
5 *Nano* **2012**, *6*, 3214–3223.  
6  
7  
8  
9 (44) Marrani, A. G.; Novelli, V.; Sheehan, S.; Dowling, D. P.; Dini, D. Probing the Redox  
10 States at the Surface of Electroactive Nanoporous NiO Thin Films. *ACS Appl. Mater.*  
11 *Interfaces* **2014**, *6*, 143–152.  
12  
13  
14 (45) Bode, H.; Dehmelt, K.; Witte, J. Zur Kenntnis Der nickelhydroxidelektrode-I.Über Das  
15 Nickel (II)-Hydroxidhydrat. *Electrochim. Acta* **1966**, *11*, 1079–IN1.  
16  
17  
18 (46) Ratcliff, E. L.; Meyer, J.; Steirer, K. X.; Garcia, A.; Berry, J. J.; Ginley, D. S.; Olson,  
19 D. C.; Kahn, A.; Armstrong, N. R. Evidence for near-Surface NiOOH Species in  
20 Solution-Processed NiO<sub>x</sub> Selective Interlayer Materials: Impact on Energetics and the  
21 Performance of Polymer Bulk Heterojunction Photovoltaics. *Chem. Mater.* **2011**, *23*,  
22 4988–5000.  
23  
24  
25 (47) Biesinger, M. C.; Payne, B. P.; Lau, L. W. M.; Gerson, A.; Smart, R. S. C. X-Ray  
26 Photoelectron Spectroscopic Chemical State Quantification of Mixed Nickel Metal,  
27 Oxide and Hydroxide Systems. *Surf. Interface Anal.* **2009**, *41*, 324–332.  
28  
29  
30 (48) Biesinger, M. C.; Payne, B. P.; Grosvenor, A. P.; Lau, L. W. M.; Gerson, A. R.; Smart,  
31 R. S. C. Resolving Surface Chemical States in XPS Analysis of First Row Transition  
32 Metals, Oxides and Hydroxides: Cr, Mn, Fe, Co and Ni. *Appl. Surf. Sci.* **2011**, *257*,  
33 2717–2730.  
34  
35  
36 (49) Sun, Y.; Wang, Y.; Pan, J. S.; Wang, L.; Sun, C. Q. Elucidating the 4f Binding Energy  
37 of an Isolated Pt Atom and Its Bulk Shift from the Measured Surface- and Size-Induced  
38 Pt 4f Core Level Shift. *J. Phys. Chem. C* **2009**, *113*, 14696–14701.  
39  
40  
41 (50) Shyu, J. Z.; Otto, K. Identification of Platinum Phases on  $\gamma$ -Alumina by XPS. *Appl.*  
42 *Surf. Sci.* **1988**, *32*, 246–252.  
43  
44  
45  
46  
47  
48  
49  
50  
51  
52  
53  
54  
55  
56  
57  
58  
59  
60

- 1  
2  
3 (51) Beverskog, B.; Puigdomenech, I. Revised Pourbaix Diagrams for Nickel at 25–300 °C.  
4  
5 *Corros. Sci.* **1997**, *39*, 969–980.  
6  
7 (52) Mayrhofer, K. J. J.; Blizanac, B. B.; Arenz, M.; Stamenkovic, V. R.; Ross, P. N.;  
8  
9 Markovic, N. M. The Impact of Geometric and Surface Electronic Properties of Pt-  
10  
11 Catalysts on the Particle Size Effect in Electrocatalysis. *J. Phys. Chem. B* **2005**, *109*,  
12  
13 14433–14440.  
14  
15  
16  
17  
18  
19  
20  
21  
22  
23  
24  
25  
26  
27  
28  
29  
30  
31  
32  
33  
34  
35  
36  
37  
38  
39  
40  
41  
42  
43  
44  
45  
46  
47  
48  
49  
50  
51  
52  
53  
54  
55  
56  
57  
58  
59  
60

## TOC Graphic

